Volume 8 | Number 27 | 21 July 2016 | Pages 13083–13524

Nanoscale

www.rsc.org/nanoscale

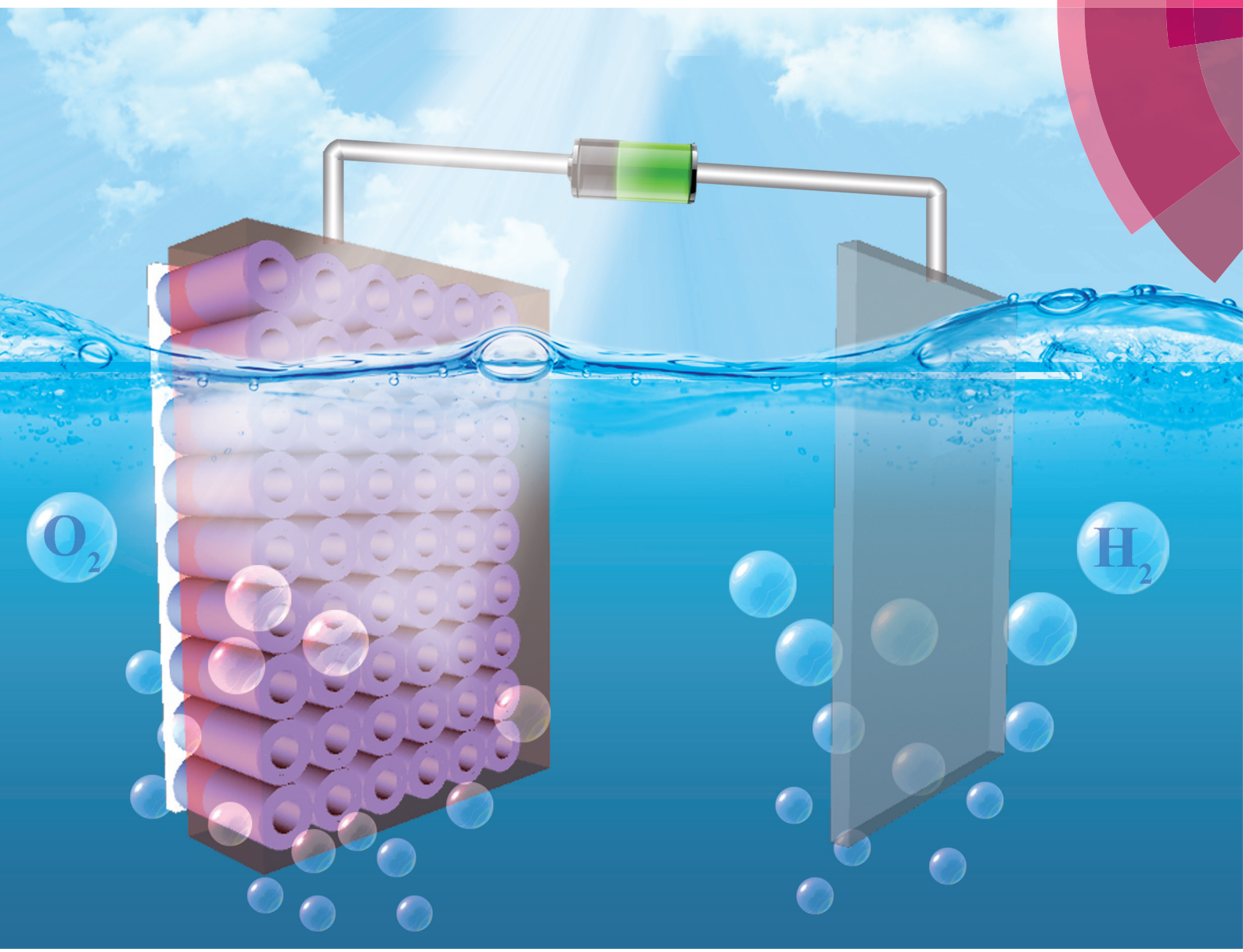

ISSN 2040-3364

ROYAL SOCIETY OF CHEMISTRY

PAPER

Lu-Ning Wang, Zheng-Hong Huang *et al.*

Facile fabrication of organic/inorganic nanotube heterojunction arrays for enhanced photoelectrochemical water splitting

NCNST

Nanoscale

PAPER

View Article Online
View Journal | View Issue

Cite this: *Nanoscale*, 2016, **8**, 13228

Facile fabrication of organic/inorganic nanotube heterojunction arrays for enhanced photoelectrochemical water splitting†

Yingzhi Chen,[a] Aoxiang Li,[a] Xiaoqi Yue,[a] Lu-Ning Wang,*[a] Zheng-Hong Huang,*[b] Feiyu Kang[b] and Alex A. Volinsky[c]

Organic/inorganic heterojunction photoanodes are appealing for making concurrent use of the highly photoactive organic semiconductors, and the efficient dielectric screening provided by their inorganic counterparts. In the present work, organic/inorganic nanotube heterojunction arrays composed of TiO_2 nanotube arrays and a semiconducting *N*,*N*-(dicyclohexyl) perylene-3,4,9,10-tetracarboxylic diimide (PDi) layer were fabricated for photoelectrochemical water splitting. In this arrayed architecture, a PDi layer with a tunable thickness was coated on anodic TiO_2 nanotube arrays by physical vapor deposition, which is advantageous for the formation of a uniform layer and an adequate interface contact between PDi and TiO_2. The obtained PDi/TiO_2 junction exhibited broadened visible light absorption, and an effective interface for enhanced photogenerated electron–hole separation, which is supported by the reduced charge transfer resistance and prolonged excitation lifetime *via* impedance spectroscopy analysis and fluorescence emission decay investigations. Consequently, such a heterojunction photoanode was photoresponsive to a wide visible light region of 400–600 nm, and thus demonstrated a highly enhanced photocurrent density at 1.23 V *vs.* a reversible hydrogen electrode. Additionally, the durability of such a photoanode can be guaranteed after long-time illumination because of the geometrical restraint imposed by the PDi aggregates. These results pave the way to discover new organic/inorganic assemblies for high-performance photoelectric applications and device integration.

Received 9th November 2015,
Accepted 16th February 2016

DOI: 10.1039/c5nr07893h

www.rsc.org/nanoscale

Introduction

Photoelectrochemical (PEC) water splitting into hydrogen and oxygen is considered one of the most promising ways to achieve photoenergy conversion, and so far considerable efforts have been devoted to improve PEC systems.[1–3] In achieving high-efficiency photoanodes, appropriate choice of semiconductor photocatalytic materials and fabrication techniques is important,[4–7] because the photophysical events (*i.e.*, sunlight absorption, exciton formation, charge carrier generation, and separation and transfer) that occur in the photoanodes, determine the system's performance. The absorption of a large fraction of sunlight is required for the photoanode system to achieve high efficiency in PEC cells under sunlight illumination. On the other hand, prompt separation of the photogenerated charge carriers is extremely important to fully utilize the photoresponse of the photoanode system.[8] In this regard, heterojunction architectures,[9] particularly in ordered geometry, are feasible and hold promise for great advances.

Nowadays, inorganic heterojunctions composed of one-dimensional (1D) nanostructured arrays have been widely explored,[10–15] because they can offer great light harvesting capability and unidirectional electrical channels for efficient charge separation and electron transport. However, most inorganic semiconductors still suffer from inefficient light absorption, and these inorganic geometry photoanodes usually require a series of complicated fabrication processes, and some steps even have to be carried out at quite high temperatures. In order to improve the sunlight utilization, organo-photoanodes made of small-molecule organic semiconductor bilayers (*i.e.*, p–n junction) have been recently found to enable water oxidation and proton reduction into hydrogen and oxygen simultaneously across the wide or even entire visible light energy region, and they are simply prepared by low temperature processing (solution processed or vapor

[a]*School of Materials Science and Engineering, University of Science and Technology Beijing, Beijing, 100083, PR China. E-mail: luning.wang@ustb.edu.cn*
[b]*Key Laboratory of Advanced Materials (MOE), School of Materials Science and Engineering, Tsinghua University, Beijing 100084, China. E-mail: zhhuang@mail.tsinghua.edu.cn*
[c]*Department of Mechanical Engineering, University of South Florida, Tampa, FL 33620, USA*

†Electronic supplementary information (ESI) available: Additional structural characterization. See DOI: 10.1039/c5nr07893h

deposition).[16–18] However, the resulting photocurrent by organo-photoanodes is often identified as having low magnitude (μA cm^{-2}) when no sacrificial reagents are added because of their low charge-carrier mobility. Alternatively, the organic/inorganic heterojunction is characterized by unique features.[19,20] It can take advantage of the superior intrinsic carrier mobility brought about by the inorganic component, as well as the great variety, broad sunlight absorption and easy functionality *via* molecular design of these small-molecule organic semiconductors.[21–23] Semiconducting polymers in conjunction with inorganic nanostructures have already been developed as photoelectric devices.[24–26] However, there are few reports about 1D inorganic arrays hybridizing with small-molecule and highly photoactive organic semiconductors as photoanodes in PEC applications. Therefore, it is desirable to fabricate these arrayed organic/inorganic assemblies for high-performance PEC cells.

In the present work, we demonstrate the fabrication of organic/inorganic nanotube heterojunction arrays by physical vapor deposition (PVD) of *N*,*N*-(dicyclohexyl) perylene-3,4,9,10-tetracarboxylic diimide (PDi) aggregates on TiO_2 nanotube arrays. TiO_2 nanotube arrays still remain a favorable choice as photoanodes because of the high light confinement and high carrier mobility,[27–29] along with the low cost and stability, intrinsic in TiO_2.[30] PDi is characterized by high extinction coefficients in the visible spectrum region, photostability and ability to self-assemble into ordered nanostructures.[31–33] Its derivatives have previously been used as high mobility, air-stable n-type semiconductors and are readily modified *via* straightforward synthetic routes.[34,35] Therefore, an effective heterojunction photoanode was formed for PEC water splitting by combining TiO_2 nanotube arrays and a uniform PDi layer with an easily tunable thickness. The advantages of constructing such heterojunctions are summarized as follows. First, the highly photoactive PDi and the energy band match between PDi and TiO_2 rendered broadened visible light absorption, and an effective interface or surface beneficial for carrier generation and charge transfer, which are also strengthened by the arrayed architecture. Taking advantage of this heterojunction, great enhancement of photocurrent density was achieved at 1.23 V *vs*. reversible hydrogen electrode (RHE) without any co-catalyst or sacrificial reagents, which is superior to most reported TiO_2- or organo-based photoanodes. Second, outer PDi aggregates offered high PEC stability of this heterojunction, and 88% of the initial photocurrent thereby remained after 2 h of persistent illumination. Thus, such an arrayed architecture made of organic/inorganic heterojunctions could form the basis of a stable and efficient PEC system.

Experimental

Sample preparation

Fabrication of TiO_2 nanotube arrays. A Ti foil with a thickness of 0.25 mm was cut into 1 × 1.5 cm^2 pieces and ultrasonically rinsed with acetone, ethanol, and deionized water in sequence for 20 min. The Ti foil was then rinsed in $HF/HNO_3/H_2O$ (1 : 4 : 2 volume ratio) for 10 s to clean the surface before use. The anodization was then performed using a two-electrode cell with the Ti foil as the working electrode and a platinum foil as the counter electrode under a constant applied voltage of 60 V at room temperature for 30 min. The distance between the two electrodes was kept at approximately 2 cm. The electrolyte contained 0.2 wt% NH_4F in ethylene glycol and H_2O mixture in the volumetric ratio of 50 : 1. The as-prepared TiO_2 nanotube arrays were then rinsed with DI water, dried, and annealed at 450 °C for 30 min in air using a furnace with a heating rate of 10 °C min^{-1}.

Fabrication of PDi/TiO_2 nanotube arrays. The PVD method was adopted to coat the surface of TiO_2 nanotube arrays with a PDi film in a horizontal tube furnace. Typically, a small porcelain boat containing 3 mg of PDi powder was placed at the furnace's center, and the anodic TiO_2 samples were loaded at the downstream with certain spacing distance away from the center to collect PDi. Before heating, high-purity N_2 was introduced into the quartz tube at a constant flow of 80 mL min^{-1} for 20 min to displace the air inside. Under the N_2 flow, the furnace was then heated to 380 °C in 30 min, and maintained at that temperature for 10 min. Then, the furnace cooled naturally to room temperature. It could be observed that the depositing zone was located 20–30 cm away from the PDi powder source.

Characterization

The morphology was observed using a Hitachi S-4800 scanning electron microscope (SEM) equipped with an X-ray energy-dispersive spectrometer (EDX). Transmission electron microscopy (TEM) images were obtained using a transmission electron microscope (JEM-2100F) operated at an accelerating voltage of 200 kV. The X-ray diffraction (XRD) patterns were obtained with a Bruker D8 Focus under Cu-Kα radiation with a scanning speed of 10° min^{-1}. UV/Vis absorption spectra were recorded with a Cary 5000 Varian spectrophotometer. Fluorescence spectra were recorded using an F-4500 fluorescence spectrophotometer. Time-resolved fluorescence measurements were carried out on a Fluorescence Lifetime Spectrometer (F900).

PEC measurement

The PEC measurements were carried out on a CHI 660E potentiostat/galvanostat electrochemical analyzer in a three-electrode cell, in which the as-prepared samples were employed as the photoanodes, and platinum mesh and saturated calomel electrode (SCE) were employed as counter and reference electrodes, respectively. An aqueous solution of NaOH was used as the electrolyte (pH 8.1). The sample films (1 cm × 1.2 cm) were vertically dipped into the electrolyte and illuminated with AM 1.5 G simulated sunlight (100 mW cm^{-2}). The measured potential *versus* SCE was converted to the RHE scale according to the Nernst equation ($E_{RHE} = E_{SCE} + 0.059pH + 0.237$), where E_{RHE} is the potential *vs*. RHE, E_{SCE} is the poten-

tial *vs.* SCE, and pH is the electrolyte's pH value. The light was produced by an Oriel Sol3A solar simulator (Newport).

Results and discussion

The synthesis of the integrated photoanodes of PDi/TiO_2 is depicted in Fig. 1. The anodic TiO_2 samples worked as the depositing substrates with different spacing distances to collect PDi *via* the PVD process in a horizontal tube furnace. To ensure a homogeneous coating of PDi, the anodic TiO_2 samples were placed in the axial direction of the TiO_2 nanotube arrays parallel to the inward carrier gas flow (see Fig. S1†). Here, four pieces of anodic TiO_2 substrates were located at 30, 28, 26 and 23 cm, separately, away from the PDi powder source, and the obtained products were denoted as PDi/TiO_2 junctions I, II, III, and IV, accordingly. For comparison, individual PDi samples were obtained by replacing the TiO_2 substrate with ITO glass of the same size, and named as PDi-I, II, III, and IV in sequence.

The top surface of the TiO_2 nanotube arrays and PDi/TiO_2 junctions is shown in Fig. 2A–E. The TiO_2 nanotube arrays were observed to be vertically aligned on the entire surface of the Ti substrate with the pore diameter around 40 nm, wall thicknesses around 30 nm, and length up to 4 μm (Fig. 2A and S2†). Fig. 2B–E present the morphology differences in the PDi/TiO_2 junctions. It was not distinctly changed between junction I and the original TiO_2 nanotube arrays, whereas some aggregates were found to be formed on the surface of the TiO_2 nanotube arrays for junctions II and III until a thick aggregate layer covered the array surface of junction IV. These suggested that the loading content of PDi increased as the anodic TiO_2 substrate approached the PDi source in the deposition zone. This could also be verified by the EDX results (Fig. S3†), which compared the relative content of the C element. As Fig. S3† showed, the original TiO_2 nanotube arrays had a carbon content of about 0.75 wt%. After the PVD process, an increase of carbon content was shown for the junctions, and when the distance between the TiO_2 substrate and the PDi source was shortened to 23 cm, a high value up to 9.23 wt% was found for junction IV.

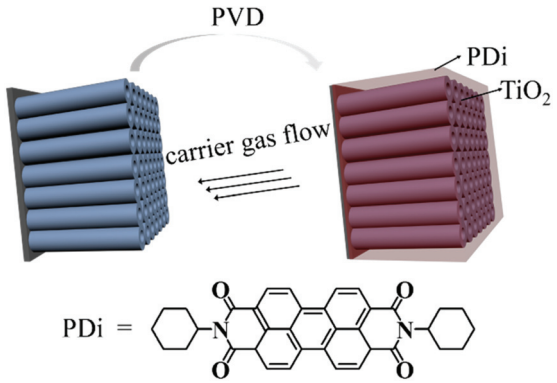

Fig. 1 Schematic illustration of the fabrication of PDi/TiO_2 junctions.

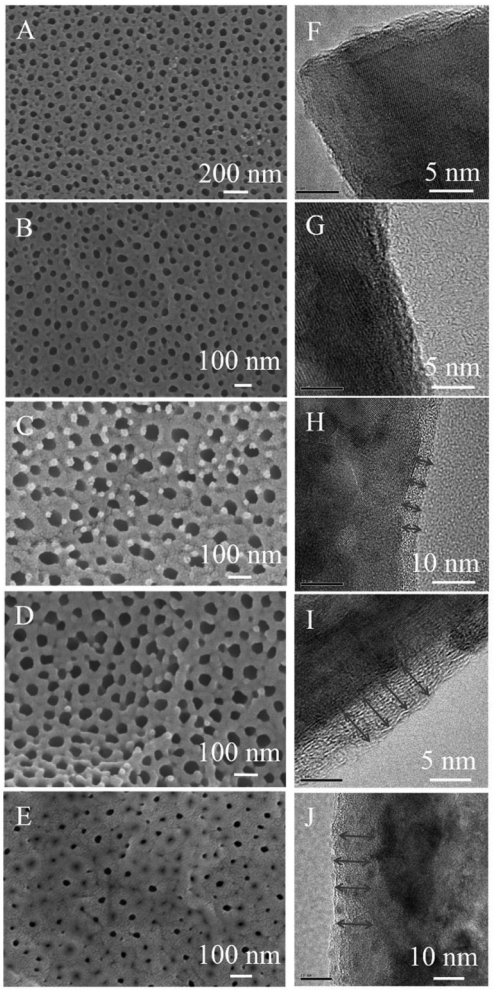

Fig. 2 SEM images of (A) TiO_2 nanotube arrays; (B) PDi/TiO_2 junctions I; (C) II; (D) III; (E) IV and (F–J) their corresponding HRTEM images in sequence.

The obtained TiO_2 nanotube arrays and PDi/TiO_2 junctions were further characterized using a high resolution (HR) TEM imaging (Fig. 2F–J), which was used to estimate the thickness of the PDi film surrounding the TiO_2 array surface. The HRTEM image in Fig. 2F first confirmed the crystal nature of the TiO_2 nanotubes. Junction I showed no significant morphology difference from TiO_2 nanotube arrays because of the very small amount of PDi deposition (Fig. 2G), but the array surfaces in junctions II–IV were definitely covered by an amorphous film that should correspond to the PDi layer (Fig. 2H–J). In detail, the thickness of the PDi layer was determined to be approximately 2, 5, and 10 nm for junctions II, III, and IV, respectively, indicating the increasing loading content of PDi from junctions I to IV. This outcome also agrees quite well with the EDX results. Since TiO_2 nanotube arrays were finely covered with the PDi film, a good electrical contact between them was attainable.

The structural integrity and the optical properties of the synthesized samples were examined by XRD (Fig. 3A) and

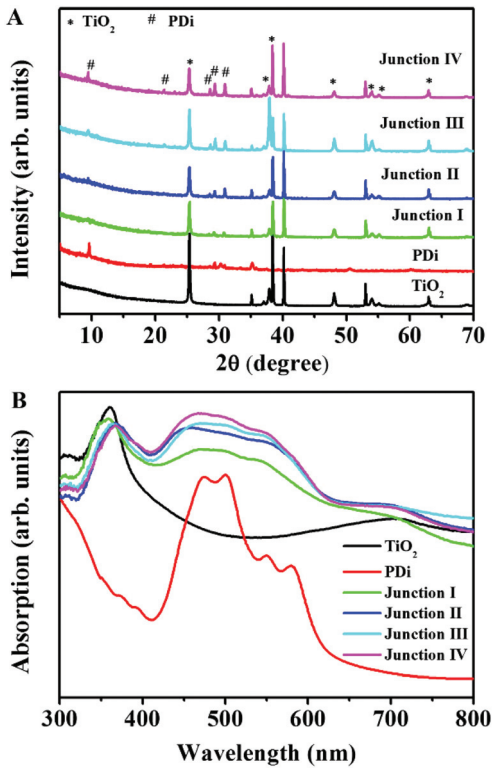

Fig. 3 (A) XRD and (B) UV-Vis absorption spectra of the synthesized samples.

UV-Vis absorption (Fig. 3B) spectra. For the anodic TiO_2 sample, the diffraction peaks at 25.3, 36.9, 37.9, 48.1, 54.0, 55.1 and 68.8° are unambiguously assigned to (101), (103), (004), (200), (105), (211) and (116) planes of anatase TiO_2 (tetragonal, *I*41/*amd*, JCPDS card no. 21-1272), and the remaining peaks arise from the Ti substrate. The XRD diagram of PDi demonstrated several diffraction peaks at 9.6, 19.2, 21.3, 28.6, and 29.3°.[32,36] On coupling, the PDi/TiO_2 junctions contained the characteristic diffraction peaks of both PDi and anatase TiO_2 (see the magnified spectrum in Fig. S4†), proving the presence of the PDi phase on the TiO_2 phase surface. Moreover, as more PDi was deposited, the peak intensity coming from PDi showed an increasing trend from junctions I to IV. The XRD patterns of the PDi/TiO_2 junctions indicate that the deposited PDi is attached to the surface of the TiO_2 nanotube arrays, which is in good agreement with the SEM and TEM investigations. The PDi film on the TiO_2 nanotubes was further corroborated by FT-IR studies (Fig. S5†). Briefly for pure PDi, the bands at 1695 cm^{-1} and 1657 cm^{-1} are assigned to the symmetric and antisymmetric stretching modes of the carbonyl groups with their transition dipole moments directed along the long and short chromophore axis, respectively. The aromatic C–H bending frequencies are solely prominent in the 1300–1000 cm^{-1} region. The out-of-plane C–H modes of the perylene ring are particularly observed in the 900–700 cm^{-1} region of the infrared spectrum.[37,38] The IR spectrum of the TiO_2 nanotubes in the range of 4000–600 cm^{-1} agrees with the reported data.[39] After deposition, IR peaks of PDi appeared, and became more obvious with the increased loading amount of PDi on the TiO_2 nanotube arrays.

The UV-Vis absorption spectra (Fig. 3B) showed that the TiO_2 nanotube arrays only absorbed light with the wavelength shorter than 400 nm, whereas PDi displayed a broad and strong absorption over the range of 400–600 nm. After hybridization, the PDi/TiO_2 junctions demonstrated an extended and enhanced absorbance that covered the absorption range from both PDi and TiO_2 along with some red shifts near 400 nm. With more PDi coverage, the peak position was red-shifted further from junctions I to IV, indicating that charge transfer occurred between PDi and TiO_2. Since the photoluminescence (PL) emission is related to the charge transfer behavior of the photoinduced electrons and holes, it can probe the excited-state interactions of PDi and TiO_2 in the junction. In the absence of TiO_2 nanotubes, individual PDi displayed strong fluorescence (FL) around 630 nm as seen from the emission spectrum of PDi (I–IV) in Fig. S6† (excited at 450 nm). For comparison, the PDi/TiO_2 junctions showed a varied degree of luminescence quenching, with the largest quenching (92%) observed for junction III. A possible pathway for the luminescence quenching of the excited PDi may be attributed to the photoinduced electron transfer between PDi and TiO_2,[40,41] which means high separation efficiency of the photogenerated electron–hole pairs.

For the PEC activity evaluation, the photocurrent density as a function of potential was first measured for all the samples under chopped illumination (100 mW cm^{-2}). As shown in Fig. 4A, a negligible current was observed during the dark cycles over the applied potential, and during light on cycles, anodic currents were measured for all the samples. At the water oxidation potential (1.23 V *vs.* RHE), PDi showed an extremely low current density of about 1 μA cm^{-2} (see the magnified spectrum in Fig. S7†), which was ascribed to its low electron mobility. The current density of the bare TiO_2 nanotube array photoanode reached 0.31 mA cm^{-2} at 1.23 V *vs.* RHE, and when it was paired with PDi, the PDi/TiO_2 junctions generated higher photocurrent density than bare TiO_2 samples. The outperformance of PDi/TiO_2 junctions can be interpreted by the broadened light absorption and spatial photocharge transfer between PDi and TiO_2. Also, higher photocurrent density means that more photoinduced electrons could be transferred from the photoanode to the counter electrode *via* an external circuit. In detail, the photocurrent density was determined to be about 0.36, 0.39, and 0.74 mA cm^{-2} at 1.23 V *vs.* RHE for junctions I, II, and III, correspondingly, with the best performance available in junction III. Junction IV instead displayed a lower current density than junction III, possibly because the excessive coverage of PDi film on the TiO_2 nanotube arrays partially blocked the surface pores and thereby hindered the electrolyte from entering the inner tubes, thus making the electron transfer at the photoanode/electrolyte interface greatly reduced. Nevertheless, the PDi/TiO_2 junction, especially junction III, demonstrated an enhanced photocurrent generation at 1.23 V *vs.* RHE without any co-catalyst or

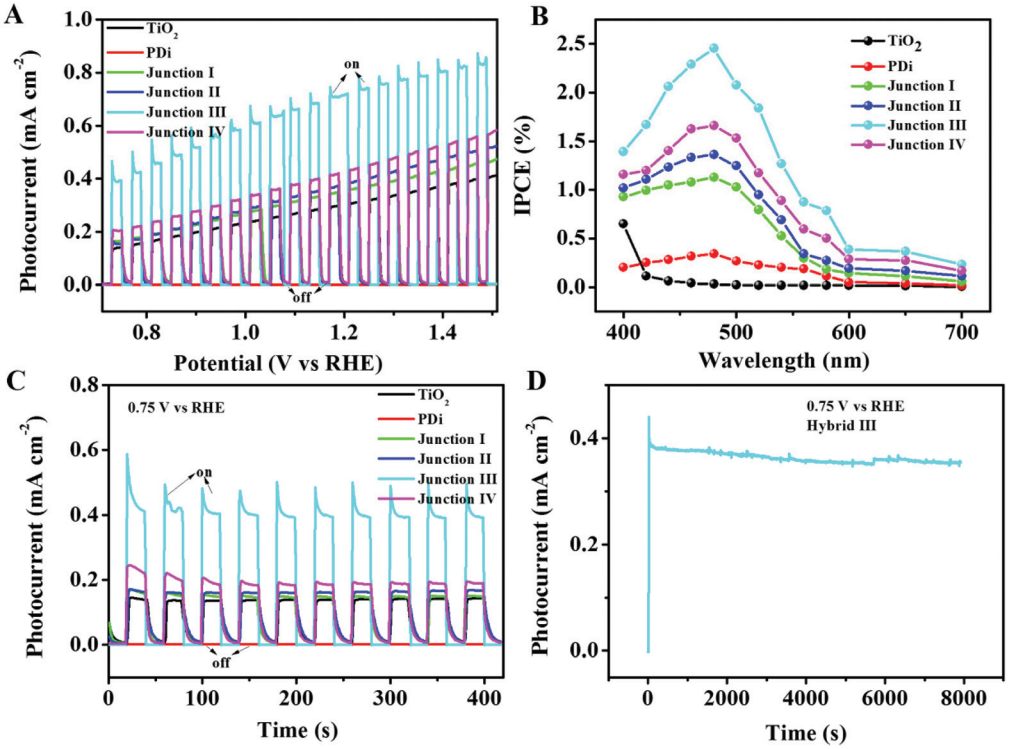

Fig. 4 (A) Photocurrent *vs*. applied potential under chopped illumination; (B) IPCE plots in the 400–700 nm range at 1.23 V *vs*. RHE, and (C) photocurrent *vs*. time plots at 0.75 V *vs*. RHE under chopped illumination for the synthesized samples; (D) time courses for the photocurrent densities of junction III at 0.75 V *vs*. RHE. All measurements were carried out in NaOH solution (8.1 pH) under 100 mW cm^{-2} illumination.

sacrificial reagents compared with most TiO_2- or organo-photoanodes previously reported.[42–46]

Incident photon-to-current-conversion efficiency (IPCE) measurements were further performed at 1.23 V *vs*. RHE to evaluate the photoactivity of the prepared photoanodes. IPCE values were calculated using the following equation and are presented in Fig. 4B as a function of the incident light wavelength (400–700 nm):

$$\mathrm{IPCE} = \frac{1240I}{\lambda J_{\mathrm{light}}} \times 100\%$$

Here, I is the photocurrent density (mA cm^{-2}), J_{light} is the incident light irradiance (mW cm^{-2}), and λ is the incident light wavelength (nm). In comparison to the bare TiO_2 sample, PDi/TiO_2 junctions are responsive to a wide spectrum range of 400–600 nm. The IPCE values increased in the following order: TiO_2 < junction I < junction II < junction IV < junction III. In particular, increasing IPCE values were observed in the wavelength regions of PDi. Based on this, an analogous conclusion on the photocurrent generation for the several samples can also be deduced under visible light irradiation (λ > 400 nm).

The photocurrent *versus* time plot for all samples at a constant potential of 0.75 V *vs*. RHE under illumination (100 mW cm^{-2}) is given in Fig. 4C. Likewise, the PEC performance of the samples followed the same order: junction III (*ca*. 0.4 mA cm^{-2}) > junction IV > junction II > junction I > TiO_2 nanotube arrays > PDi as that in Fig. 4A, and emphasized the importance of integration of PDi with the TiO_2 nanotube arrays. Additionally, there was no obvious decline in the current density for all junctions after several cycles. Regarding the greatest enhancement of photocurrent generated by junction III, the steady-state photocurrent was tested under the same conditions, shown in Fig. 4D. It was found that the steady-state photocurrent density of junction III was almost equal to its photocurrent density in Fig. 4C. Moreover, about 88% of the initial photocurrent remained after 8000 s illumination at 0.75 V *vs.* RHE for junction III, indicating the stability and the intimate interfacial contact in the PDi/TiO_2 junctions. FT-IR analysis was further used to measure its photostability. As shown in Fig. S8,† junction III after long-time illumination displayed little difference from its original state either from peak position or peak intensity, and thereby indicated its reliability as a photoanode.

Electrochemical impedance spectroscopy (EIS), a powerful tool to study charge transfer processes inside the photoanode and at the interface between the photoanode and electrolyte, was used to investigate the separation efficiency of the charge carriers. The impedance was measured at the frequency range of 0.1–10^6 Hz using an amplitude of 10 mV at 1 V *vs*. RHE. The EIS results are presented in Fig. 5A as Nyquist plots, where *x*- and *y*-axes are the real part (Z') and the negative of imaginary part ($-Z''$) of impedance. In general, a large value of impedance indicates poor conductivity along the electron pathway in the electrode, and the fitting of raw data to an equivalent

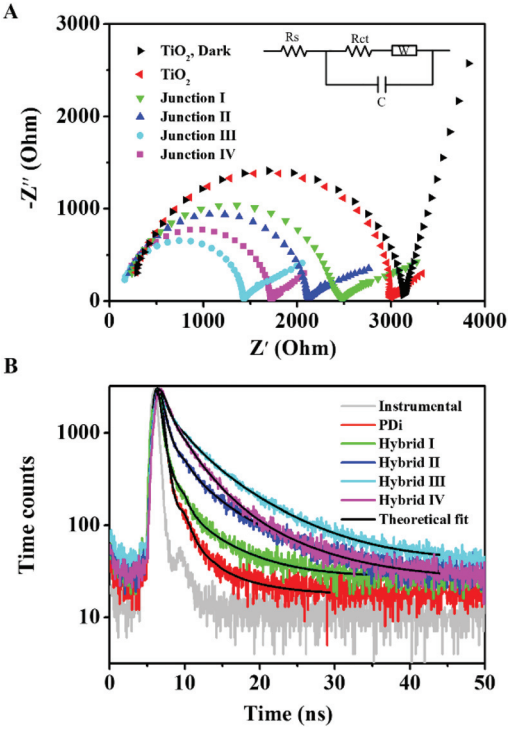

Fig. 5 (A) The Nyquist plot measured in NaOH solution (8.1 pH) at 1 V applied potential *vs.* RHE under illumination at 100 mW cm^{-2} for various photoanodes, and the inset is the equivalent circuit model; (B) the FL decay profiles of the photoanodes (λ_{ex} = 450 nm, λ_{mon} = 600 nm) along with the fitted curves.

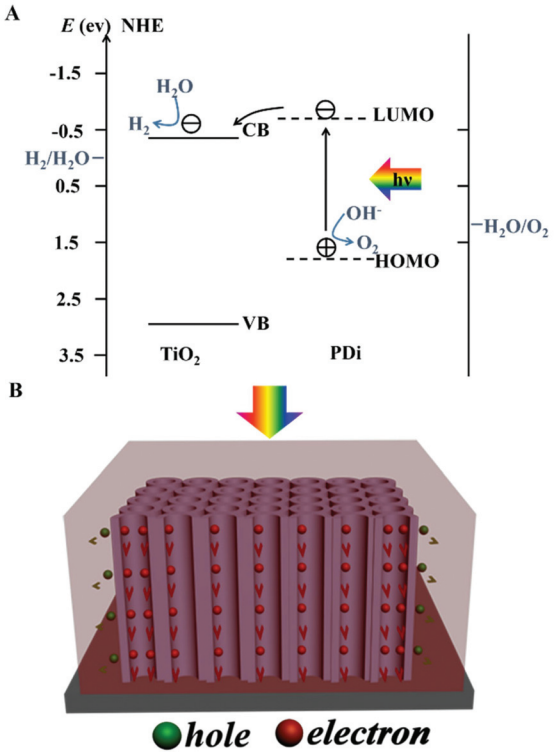

Fig. 6 Schematic illustration of: (A) energy diagram and (B) expected charge flow in the PDi/TiO_2 junction photoanode.

circuit model is thereby performed for the EIS analysis, as shown in the inset of Fig. 5A. Here, R_s refers to the total series resistance that is the intersection of the diagram with the *x*-axis. R_{ct} is the charge transfer resistance of the interfaces inside the photoanode and at the photoanode/electrolyte interfaces that correspond to the diameter of the arch. Clearly, the arch for TiO_2 nanotube arrays under illumination is smaller than that for TiO_2 in the dark. Also, TiO_2 sample showed the largest impedance among the various photoanodes under illumination. It can be seen that when PDi was introduced into the TiO_2 system, the arch decreased to a large extent, implying that the PDi/TiO_2 junction could significantly reduce the charge transfer resistance. Furthermore, with the increasing amount of PDi, the arch decreased first and then increased. The smallest arch (or R_{ct}) was observed in junction III. Table S1† also summarizes the quantitatively fitted results based on the equivalent circuit. The arch size in Fig. 5A has the tendency of increasing the R_{ct} value for the samples (Table S1†). For example, the R_{ct} value was estimated to be 2738 Ω for TiO_2, and decreased to 2156, 1905, 1290, and 1564 Ω for junctions I–IV, accordingly. As a result of lower R_{ct} values, charge carrier recombination should be more suppressed, and the spatial charge carrier separation is thereby facilitated.

To gain deeper insight into the charge carrier separation, we monitored the PDi emission decays of the PDi-based photoanodes by using a time-correlated single-photon counting (TCSPC) technique (Fig. 5B). The excitation and monitoring wavelengths are 450 and 600 nm, respectively. Overall, the decay kinetics of PDi/TiO_2 junctions became slow compared with PDi itself. This indicates that the transfer of photogenerated electrons and holes is improved in the PDi/TiO_2 junctions, which can retard the recombination probability of charge carriers. Here, a bi-exponential decay model was needed to obtain acceptable fits, and the fitted FL lifetime is summarized in Table S2.† In detail, the average FL lifetime ($<\tau>$) was estimated to be *ca.* 0.9 ns for PDi, but increased to 1.29, 3.18, 4.60, and 3.57 ns for junctions I–IV, accordingly. These results are in line with the EIS results. It is also worth noting that the longest FL lifetime and the smallest R_{ct} exhibited by PDi/TiO_2 junction III remarkably promoted the charge carrier separation and charge transfer, and thus explained its highest photocurrent generation.

The working principle of this PDi/TiO_2 junction photoanode is illustrated in terms of the energy diagram presented in Fig. 6A. TiO_2 has the conduction band (CB) edge (E_{CB} = −3.8 eV) that lies below the LUMO band of PDi (E_{LUMO} = −4.2 eV). In this system, PDi works as the central photocatalyst that responds to visible light. The 1D nanotube arrays can decrease light reflection to bring more efficient utilization of the incoming light. When photoexcited, PDi absorbs photons, and electrons and holes are generated. The photogenerated electrons then move rapidly to the Pt counter electrode for the

H_2O/H_2 reaction, by way of the unidirectional electron channels provided by the TiO_2 nanotube arrays (Fig. 6B), according to the potential difference of the two semiconductors. Holes left in the HOMO of PDi are then transported away to the solution for the H_2O/O_2 reaction. Consequently, the generated electron–hole pairs are effectively separated and transferred. Thus, efficient charge separation can be rendered across the arrayed junction structure, which improves its PEC water splitting activity.

Conclusions

In summary, organic/inorganic nanotube heterojunction arrays were fabricated by coating the surface of the TiO_2 nanotube arrays with PDi film *via* the PVD method. The coated PDi film was uniform and the thickness could be tuned simply by adjusting the collecting distances. The resultant PDi/TiO_2 junction photoanodes were responsive to a wide visible-light region (400–600 nm), and demonstrated enhanced photocurrent density derived from PEC water splitting, compared with each component. The integration of the PDi aggregate layer and TiO_2 nanotube arrays brought the dramatic performance improvement by prolonging the carrier lifetime and reducing charge transfer resistance for efficient charge separation and electron transfer across the formed junction structure, as well as by increasing the sunlight absorption. The PDi/TiO_2 junctions also afforded high PEC stability for persistent illumination due to geometrical restraints by the formation of organic aggregates. Our results have demonstrated promising strategies for designing and constructing small-molecule organic/inorganic heterojunction photoelectrodes for practical sunlight-driven PEC water splitting.

Acknowledgements

The authors are grateful to the National Natural Science Foundation of China (Grant No. 51503014), and the Beijing Higher Education Young Elite Teacher Project (No. YETP0419).

Notes and references

1 Q. Liu, J. He, T. Yao, Z. Sun, W. Cheng, S. He, Y. Xie, Y. Peng, H. Cheng and Y. Sun, *Nat. Commun.*, 2014, **5**, 5122.
2 E. Miller, *Energy Environ. Sci.*, 2015, **8**, 2809.
3 T. Hisatomi, J. Kubota and K. Domen, *Chem. Soc. Rev.*, 2014, **43**, 7520.
4 X. Wang, C. Liow, A. Bisht, X. Liu, T. C. Sum, X. Chen and S. Li, *Adv. Mater.*, 2015, **27**, 2207.
5 X. Wang, M. Xi, H. Fong and Z. Zhu, *ACS Appl. Mater. Interfaces*, 2014, **6**, 15925.
6 J. Deng, X. Lv, J. Liu, H. Zhang, K. Nie, C. Hong, J. Wang, X. Sun, J. Zhong and S.-T. Lee, *ACS Nano*, 2015, **5**, 5348.
7 C. C. Nguyen, N. N. Vu and T.-O. Do, *J. Mater. Chem. A*, 2015, **3**, 18345–18359.
8 S. G. Babu, R. Vinoth, D. Praveen Kumar, M. V. Shankar, H.-L. Chou, K. Vinodgopal and B. Neppolian, *Nanoscale*, 2015, **7**, 7849.
9 M. Reza Gholipour, C.-T. Dinh, F. Beland and T.-O. Do, *Nanoscale*, 2015, **7**, 8187.
10 G. Ai, H. Li, S. Liu, R. Mo and J. Zhong, *Adv. Funct. Mater.*, 2015, **25**, 5706.
11 J. Hou, C. Yang, H. Cheng, S. Jiao, O. Takeda and H. Zhu, *Energy Environ. Sci.*, 2014, **7**, 3758.
12 X. Wang, C. Liow, D. Qi, B. Zhu, W. R. Leow, H. Wang, C. Xue, X. Chen and S. Li, *Adv. Mater.*, 2014, **26**, 3506.
13 F. X. Xiao, J. Miao, H. B. Tao, S. F. Hung, H. Y. Wang, H. B. Yang, J. Chen, R. Chen and B. Liu, *Small*, 2015, **11**, 2115.
14 F.-X. Xiao, Z. Zeng and B. Liu, *J. Am. Chem. Soc.*, 2015, **137**, 10735.
15 F. X. Xiao, S. F. Hung, J. Miao, H. Y. Wang, H. Yang and B. Liu, *Small*, 2015, **11**, 554.
16 T. Abe, N. Taira, Y. Tanno, Y. Kikuchi and K. Nagai, *Chem. Commun.*, 2014, **50**, 1950.
17 T. Abe, J. Chiba, M. Ishidoya and K. Nagai, *RSC Adv.*, 2012, **2**, 7992.
18 T. Abe, Y. Tanno, N. Taira and K. Nagai, *RSC Adv.*, 2015, **5**, 46325.
19 C. Draxl, D. Nabok and K. Hannewald, *Acc. Chem. Res.*, 2014, **47**, 3225.
20 X. Wang, W. Song, B. Liu, G. Chen, D. Chen, C. Zhou and G. Shen, *Adv. Funct. Mater.*, 2013, **23**, 1202.
21 H. Katz, A. Lovinger, J. Johnson, C. Kloc, T. Siegrist, W. Li, Y.-Y. Lin and A. Dodabalapur, *Nature*, 2000, **404**, 478.
22 Y. Chen, Z.-H. Huang, M. Yue and F. Kang, *Nanoscale*, 2014, **6**, 978.
23 S. R. Forrest and M. E. Thompson, *Chem. Rev.*, 2007, **107**, 923.
24 Y. S. Kwon, J. Lim, H.-J. Yun, Y.-H. Kim and T. Park, *Energy Environ. Sci.*, 2014, **7**, 1454.
25 Y. Guo, C. Liu, K. Inoue, K. Harano, H. Tanaka and E. Nakamura, *J. Mater. Chem. A*, 2014, **2**, 13827.
26 Y. Zhang, R. Liu, S.-T. Lee and B. Sun, *Appl. Phys. Lett.*, 2014, **104**, 083514.
27 N. Liu, C. Schneider, D. Freitag, M. Hartmann, U. Venkatesan, J. Müller, E. Spiecker and P. Schmuki, *Nano Lett.*, 2014, **14**, 3309.
28 M. Ge, C. Cao, S. Li, S. Zhang, S. Deng, J. Huang, Q. Li, K. Zhang, S. S. Al-Deyab and Y. Lai, *Nanoscale*, 2015, **7**, 11552.
29 J. Su, P. Geng, X. Li, Q. Zhao, X. Quan and G. Chen, *Nanoscale*, 2015, **7**, 16282.
30 B. Cai, D. Zhong, Z. Yang, B. Huang, S. Miao, W.-H. Zhang, J. Qiu and C. Li, *J. Mater. Chem. C*, 2015, **3**, 729.
31 C. Ramanan, A. L. Smeigh, J. E. Anthony, T. J. Marks and M. R. Wasielewski, *J. Am. Chem. Soc.*, 2011, **134**, 386.
32 Y. Chen, C. Zhang, X. Zhang, X. Ou and X. Zhang, *Chem. Commun.*, 2013, **49**, 9200.
33 H. Pan, X. Zhang, Y. Yang, Z. Shao, W. Deng, K. Ding, Y. Zhang and J. Jie, *Nanotechnology*, 2015, **26**, 295302.
34 C. Huang, S. Barlow and S. R. Marder, *J. Org. Chem.*, 2011, **76**, 2386.

35 Y. Hosoi, D. Tsunami, H. Ishii and Y. Furukawa, *Chem. Phys. Lett.*, 2007, **436**, 139.
36 Y. Che, X. Yang, K. Balakrishnan, J. Zuo and L. Zang, *Chem. Mater.*, 2009, **21**, 2930.
37 D. Ambrosek, H. Marciniak, S. Lochbrunner, J. Tatchen, X.-Q. Li, F. Würthner and O. Kühn, *Phys. Chem. Chem. Phys.*, 2011, **13**, 17649.
38 A. Menikh and A. Bouraoui, *J. Mol. Struct.*, 1997, **403**, 189.
39 K. Onozuka, B. Ding, Y. Tsuge, T. Naka, M. Yamazaki, S. Sugi, S. Ohno, M. Yoshikawa and S. Shiratori, *Nanotechnology*, 2006, **17**, 1026.
40 W. J. Beek and R. A. Janssen, *J. Mater. Chem.*, 2004, **14**, 2795.
41 D. Baskaran, J. W. Mays, X. P. Zhang and M. S. Bratcher, *J. Am. Chem. Soc.*, 2005, **127**, 6916.
42 S. Ho-Kimura, S. J. Moniz, A. D. Handoko and J. Tang, *J. Mater. Chem. A*, 2014, **2**, 3948.
43 S. Y. Chae, P. Sudhagar, A. Fujishima, Y. J. Hwang and O.-S. Joo, *Phys. Chem. Chem. Phys.*, 2015, **17**, 7714.
44 S. Zhang, R. Sakai, T. Abe, T. Iyoda, T. Norimatsu and K. Nagai, *ACS Appl. Mater. Interfaces*, 2011, **3**, 1902.
45 T. Abe, S. Tobinai, N. Taira, J. Chiba, T. Itoh and K. Nagai, *J. Phys. Chem. C*, 2011, **115**, 7701.
46 T. Abe, Y. Hiyama, K. Fukui, K. Sahashi and K. Nagai, *Int. J. Hydrogen Energy*, 2015, **40**, 9165.